Multiarray Biosensor for Diagnosing Lung Cancer Based on Gap Plasmonic Color Films

Thanh Mien Nguyen,[¶] Jae Heun Chung,[¶] Gyeong-Ha Bak,[¶] You Hwan Kim, Minjun Kim, Ye-Ji Kim, Ryuk Jun Kwon, Eun-Jung Choi, Kwang Ho Kim,* Yun Seong Kim,* and Jin-Woo Oh*

Cite This: *ACS Sens.* 2023, 8, 167−175

Read Online

ACCESS | Metrics & More | Article Recommendations | Supporting Information

ABSTRACT: Adaptable and sensitive materials are essential for the development of advanced sensor systems such as bio and chemical sensors. Biomaterials can be used to develop multifunctional biosensor applications using genetic engineering. In particular, a plasmonic sensor system using a coupled film nanostructure with tunable gap sizes is a potential candidate in optical sensors because of its simple fabrication, stability, extensive tuning range, and sensitivity to small changes. Although this system has shown a good ability to eliminate humidity as an interferant, its performance in real-world environments is limited by low selectivity. To overcome these issues, we demonstrated the rapid response of gap plasmonic color sensors by utilizing metal nanostructures combined with genetically engineered M13 bacteriophages to detect volatile organic compounds (VOCs) and diagnose lung cancer from breath samples. The M13 bacteriophage was chosen as a recognition element because the structural protein capsid can readily be modified to target the desired analyte. Consequently, the VOCs from various functional groups were distinguished by using a multiarray biosensor based on a gap plasmonic color film observed by hierarchical cluster analysis. Furthermore, the lung cancer breath samples collected from 70 healthy participants and 50 lung cancer patients were successfully classified with a high rate of over 89% through supporting machine learning analysis.

KEYWORDS: *lung cancer diagnosis, breath analysis, volatile organic compounds (VOCs), gap plasmonic resonance, M13 bacteriophage*
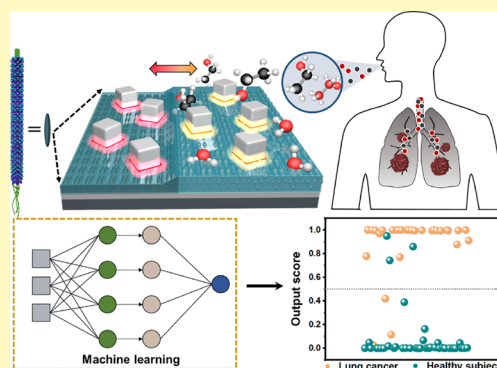
P lasmonic effects in noble metal nanostructures are probably one of the most widely recognized forms of nanotechnology that has been stipulated by efforts to condense the underlying physics and properties of localized surface plasmon resonance (LSPR).[1,2] Owing to advantages in real-world applications, such as high sensitivity, real-time monitoring, fast response time, and volume samples, plasmonic sensing based on the LSPR technique has emerged as an analytical technique in various applications, from medical diagnosis to environmental pollution monitoring.[3−6]

One of the most exciting plasmonic fields is plasmonic resonance using a coupled system with tunable gap sizes. This is getting increasing attention because of its strong electromagnetic (EM) near-field confinement and enhancement in nanogaps.[7−13] Furthermore, the coupling between the nanoparticle on the metal film (nanoparticle on mirror, NPoM) highlights the plasmonic nanostructure control compared to other coupled plasmonic nanostructures.[10,12,14] Recently, the ultrahigh local EM field enhancement of NPoM has been achieved, in which the LSPR of nanoparticles is excited by extended surface plasmons (ESPs) of the metal film, which propagates EM surface waves oscillating along the interface between a dielectric and a metal.[15−17] Although ESP-LSPR coupling configurations can exhibit ultrahigh local EM field

enhancement, it requires a special coupling medium such as a prism, wavelength, and grating.[17] Therefore, the excitation of LSPR in NPoM geometry by direct excitation from free space that can be fabricated using a simple low-cost method is a promising approach for practical applications.

NPoM has a high near-field enhancement and strong gap dependence because of the additional surface charge contribution from the metal film at a small gap size compared to nanoparticle−nanoparticle coupling.[12] The nanogap distance between the nanoparticle and the metal film plays an essential role in the constructive or destructive interference between the light scattered from the NP and the light reflected from the film, which considerably changes the wavelength and intensity of plasmon resonance.[18,19] Generally, the coupling strength of nanostructures on metal films depends on the size, shape, dielectric layer medium, and gap between the metal particles.[20,21]
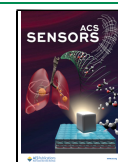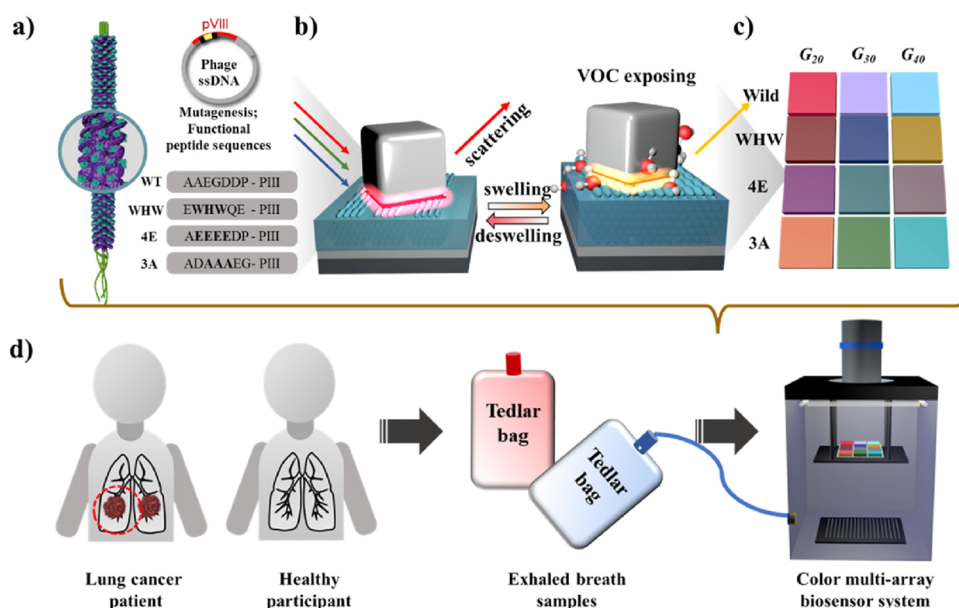
Figure 1. Schematic of the multiarray biosensor and working principle. (a) Genetically engineered M13 phage structure (left) and DNA sequencing (right). (b) Schematic of color-switching mechanism under molecular gas absorption based on gap plasmonic film using the M13 layer. (c) Schematic of the colorimetric multiarray biosensor with four genetically engineered phages (WT, WHW, 4E, and 3A) and different gap sizes (20, 30, and 40 nm). (d) Workflow of the lung cancer diagnosis. Schematic of lung cancer breath detection workflow from 50 patients and 70 healthy participants.

Taking advantage of these properties, recent research has attempted to control dynamically and reversibly the gap distance structure in diverse applications such as humidity sensing,[22−24] biomedicine,[3,25−27] and display electronics,[5,28] based on various materials and methods such as physical, chemical, and external stimulation.[22,29−31] While the dynamic plasmonic nanostructures have fantastically responded to external stimuli to change their structural properties and optical characteristics, the fabrication of plasmonic nanostructures requires complex architectures and multistep chemical functionalization. Thus, the practical applications of dynamic plasmonic nanostructures are limited. Consequently, investigation into next-generation materials requires a flexible response under diverse environments, simple fabrication, and low cost, which are still challenging.[2,32]

Recently, biological materials such as M13 bacteriophages have been used as a promising natural resource to construct multifunctional nanoscale materials in various applications, including gas sensing,[33−38] tissue regeneration,[39] and harvesting energy applications.[40] The M13 bacteriophage has been demonstrated as a biological building block with unique features known as the biomimetic self-templating processes.[41−43] Recently, a color array film based on 20 types of genetically engineered M13 bacteriophages was fabricated to classify lung cancer patients and healthy participants.[44] Although limited in terms of time-consuming fabrication methods and classification accuracy, a color array film demonstrates the highly sensitive detection ability of M13 bacteriophages and their great potential for lung cancer diagnosis. Lately, the M13 bacteriophage has been reported as an actuator to tune the gap between the Ag cube and metal film under external moisture.[45] These results demonstrated the sensitivity and stability of the biosensor based on the gap plasmonic resonance phenomenon. Therefore, inheriting and developing the application of M13 bacteriophages as a dielectric layer in the plasmonic coupled system based on

the rapid adaptability in complex environmental conditions to diagnose cancer diseases are required.

Herein, we present a controllable gap plasmonic color film (GPCF) that serves as a biosensor for volatile organic compounds (VOCs) and lung cancer detection using an actuator of an M13 bacteriophage layer as a dielectric material between Ag nanocubes positioned on Ag films. In this structure, the roles of the genetically engineered M13 bacteriophages have been demonstrated in the dielectric layer to enhance the localized EM fields and the bioreceptors in the GPCF to detect toxic gases and lung cancer diseases. The multiarray biosensor based on the GPCF was achieved, and it contained 12 substrates generated by varying the four types of genetically engineered phages and various gap sizes (Figure 1). A total of 120 human breath samples were collected from clinical diagnoses, including 50 lung cancer patients and 70 healthy participants, to examine the sensitivity of the multiarray biosensor system. With the support of machine learning analysis, the classification success rate of our sensor exhibited a high accuracy of over 89%

■ RESULTS AND DISCUSSION

Gap Plasmonic Film Fabrication and Working Principle. A flexible functional property of the capsid surface on M13 bacteriophages is a unique approach to improve the sensing performance of biosensors. To boost the sensitivity and selectivity of the GPCF film based on the M13 bacteriophage layer, the M13 bacteriophages were genetically engineered to obtain unique structures with different chemical compositions from the wild-type bacteriophage. Using biotechnology techniques in gene modification to create desired proteins with flexible and adaptable properties is one of the core characteristics of developing advanced sensor systems compared to other materials. Moreover, the development of sensing systems that can detect various targets plays a significant role in selecting and separating substances. To
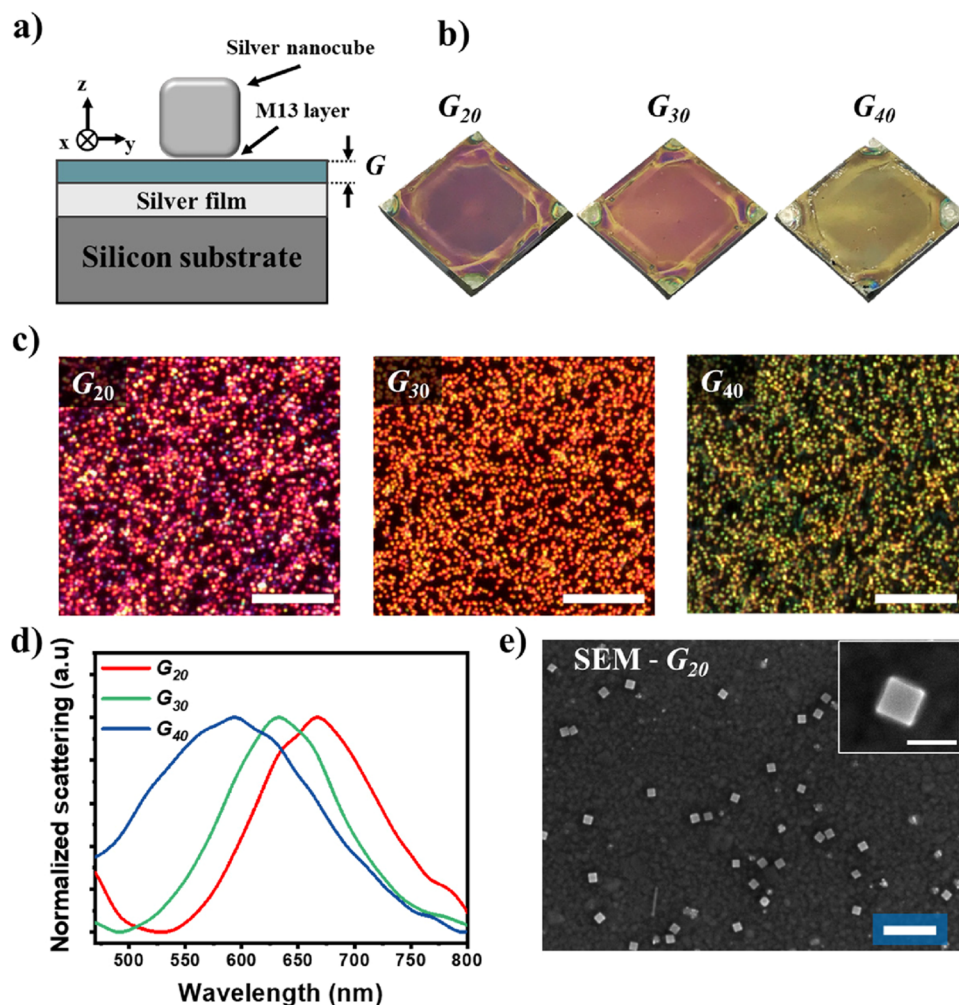
Figure 2. Gap plasmonic resonance color film properties. (a) Schematic of the geometry of the Ag nanocubes over the Ag film. (b) Actual color images of gap plasmonic film of 1 cm × 1 cm at various gaps: 20, 30, and 40 nm. (c) Optical DF images of Ag nanocubes on the Ag film separated by the M13 layer, scale bar: 2 μm. (d) DF scattering spectra of the gap plasmonic color film. (e) SEM image of the gap plasmonic film, scale bar: 500 nm. Inset image, scale bar: 100 nm.

realize these capabilities, the three genetically engineered bacteriophage-modified protein surfaces with tryptophan (W), glutamic acid (E), and alanine (A) in the 20 common amino acids act as receptors for $\pi-\pi$ stacking interaction, charge interaction, and hydrophobic interaction, respectively (Figure 1a). Using site-directed mutagenesis PCR techniques, the pVIII protein of the wild-type was controlled to yield the desired strains with WHW, EEEE, and 3A and was examined using a DNA sequencing facility (COSMO genetic CO., Korea) (Figure S11).

The color change of the GPCF produced from varying the dielectric thickness is based on the swelling and deswelling of the M13 bacteriophage layer when excited by external influences (Figure 1b). Once the thickness changes, the distance between the Ag nanocubes and the Ag metal film increases and thus causes a shift in the scattering wavelength. For each stimulus, the interaction of the M13 layer is different and makes the color change distinct.[45]

The M13 bacteriophage biomaterial layers were thinly coated with thicknesses of 10, 20, 30, and 40 nm (in short of known as G_{10}, G_{20}, G_{30}, and G_{40}, respectively), confirmed by the results of the atomic force microscopy (AFM) measurement (Figure S1). In addition, the swelling of the M13

bacteriophage was determined under moisture stimulation (Figure S2). Except for the case of G_{10}, where the swelling is low and is approximately the same as that of a monolayer of the M13 bacteriophage (6.6 nm), the M13 bacteriophage layers at G_{20}, G_{30}, and G_{40}, which enable high swelling capacity, were selected to fabricate the GPCF for biosensor applications.

Recently, colorimetric array techniques have been widely used to detect chemicals with digital images because of fast detection characteristics, simplicity of operation, and low cost. Consequently, a colorimetric multiarray based on the plasmonic color film was developed using 12 samples based on four types of bacteriophage-modified protein surfaces (WHW, 4E, 3A, and wild-type) combined with varying film array thicknesses of 20, 30, and 40 nm gap sizes for each species (Figure 1c).

Our approach was used to diagnose lung cancer which is one of the common cancers, based on the VOC gas detection from exhaled breath samples to classify lung cancer patients and healthy participants. Breath samples collected from lung cancer patients and healthy participants were analyzed according to a simple procedure. Afterward, the detecting process between the multiarray biosensor and breath sample was conducted in a home-built system (Figure 1d).
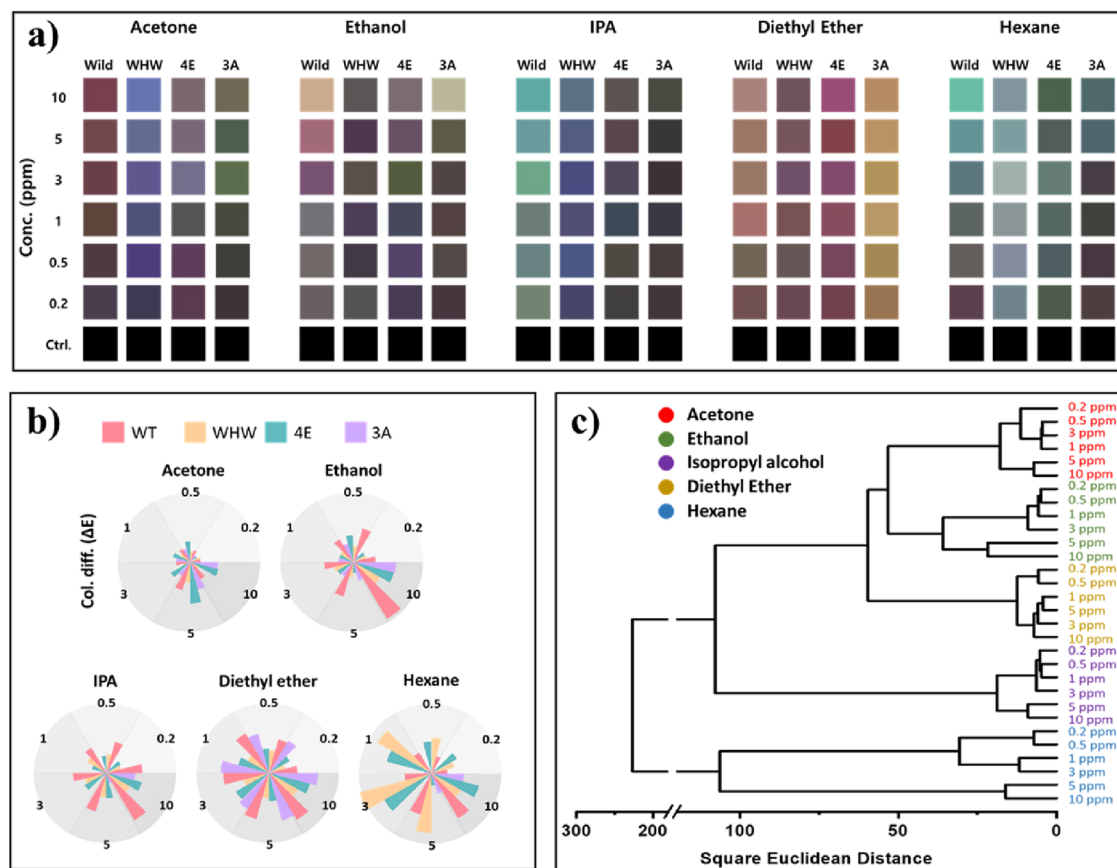
Figure 3. VOC sensing measurement using a multiarray biosensor. (a) Color palette arrays with different chemical substances and concentrations based on ΔRGB intensity. (b) Fingerprint patterns calculated by color difference (ΔE) at various concentrations (0.2, 0.5, 1, 3, 5, 10 ppm). (c) Hierarchical cluster analysis of multiarray biosensors with varying VOCs and concentrations.

The controllable GPCF was fabricated, as illustrated in Figure 2. In this geometry, the M13 bacteriophage layer acts as a dielectric spacer and was self-assembled onto a thin Ag film with a 100 nm thickness via electron-beam deposition. The M13 nanostructures act as actuators of the system to separate Ag nanocubes (75 nm) from the Ag mirror film and tune the gap size under stimuli environment conditions to enhance plasmonic resonance effectively. By varying the M13 bacteriophage concentration, the samples with different gap sizes from G_{20}, G_{30}, and G_{40} were achieved using a simple spin-coating method. Interestingly, the actual color images of the gaps in the plasmonic film were observed with the naked eye under room conditions, as illustrated in Figure 2b.

The vibrant colors are because of the plasmonic resonance effect of Ag nanocubes on Ag films separated by a small gap (as the NPoM structure mentioned). The color of the samples is blue-shifted and gradually shifts from pink to yellow as the gap increases at G_{30} and G_{40}, respectively. It is shown that the color change of the films is strongly dependent on the gap size between the Ag nanocubes and the Ag mirror film. To account for the actual color change of the gap plasmonic films produced by Ag nanocubes and Ag films at various gap sizes, the dark-field (DF) images and scattering spectra of the Ag particles were investigated, as illustrated in Figure 2c,d. From the DF images in Figure 2c, we can see that the scattering of Ag nanocubes is blue-shifted when the gap is large. In addition, the DF scattering spectra indicate specifically that the scattering resonance spectrum at the G_{20} is 675 nm and gradually decreases to 580 nm at the G_{40}. These results are

consistent with predicting about the blue-shifted scattering when the dielectric gap increases in the plasmonic coupling system between Ag nanocubes and metal films, which has been shown in a previous study.[23] Therefore, we believe that the plasmonic color film gap (Figure 2b) is generated by scattering resonance in the plasmonic coupling system between Ag nanocubes and Ag metal films. Varying the cavity distance leads to an increase and decrease of the plasmonic resonance intensity, which causes the film colors to adjust accordingly. Moreover, the Ag nanocubes on the M13 bacteriophage were characterized using scanning electron microscopy (SEM) (Figure 2e). From the SEM results, we can see that the Ag nanocubes were uniformly coated on the virus.

Gas Sensing Analysis. The human breath is a mixture of many complex gases. Distinguishing lung cancer patients and healthy participants requires a sensor system that is highly selective and sensitive to a wide range of VOCs. In the breath of lung cancer patients, >150 VOCs from many gas groups such as ancol, alkane, alkene, aromatic rings, and aldehydes have been detected.[46] Herein, more than 43 VOC biomarkers were selected to diagnose lung cancer. Therefore, the detection of various functional VOC groups can show high potential for diagnosing lung cancer breath. To test the sensitivity and selectivity of the multiarray GPCF for different gas groups, five gases (acetone, ethanol, isopropyl alcohol, diethyl ether, and hexane) were selected from different functional gas groups. The real-time measurement was performed using a home-built detection system. In the series of 12 color film matrices varying in type (WHW, 4E, 3A, and wild-type) and gap size (G_{20}, G_{30},
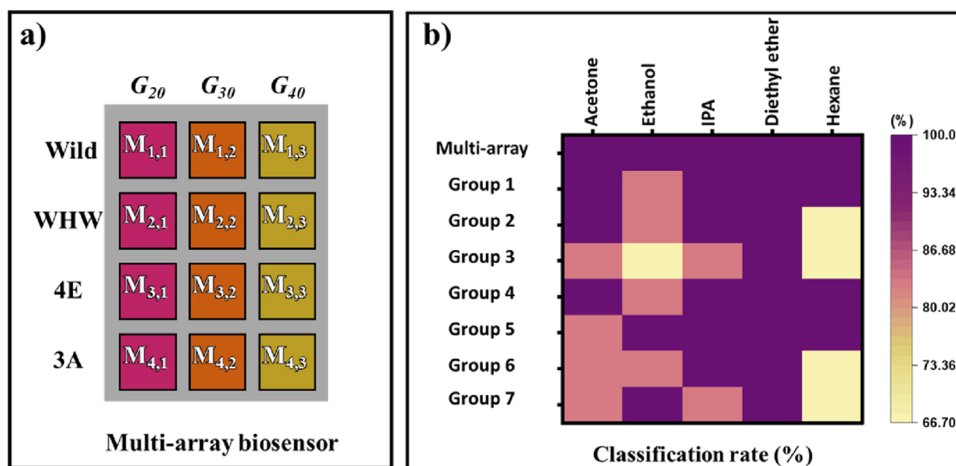
Figure 4. Comparison of the classification success rate of the bacteriophage-based biosensors. (a) Schematic of a multiarray biosensor of 4×3 matrix $(M_{i,j})$ that was divided into seven groups to calculate the classification success rate. [Group 1 = $(M_{i,1})$, Group 2 = $(M_{i,2})$, Group 3 = $(M_{i,3})$, Group 4 = $(M_{1,j})$, Group 5 = $(M_{2,j})$, Group 6 = $(M_{3,j})$, Group 7 = $(M_{4,j})$]. (b) Heatmap presented the classification success rate. All data were calculated from the HCA dendrograms of seven groups and multiple arrays.

and G_{40}), all color changes under the influence of humidity, and VOCs were recorded and analyzed as three color RGB using a CCD camera controlled by MATLAB software. Under moisture stimulation, the color palette combination displayed based on the ΔRGB intensity exhibited the different colors of multiarray biosensors and gradually varied from 20 to 90% RH with increments of 10% RH (Figure S3). Obviously, the color change was produced from the scattering resonance variation observed using the DF optical images (Figure S4). The color palette difference in each genetically engineered bacteriophage film implies that the interaction levels with different moisture levels are not the same. Consequently, various color arrays were generated to easily distinguish humidity levels.

The multiarray biosensor of the GPCF was further tested with varying concentrations of VOCs. Each genetically engineered bacteriophage carries pVIII proteins that provide a specific chemical structure and selective response to different substances. Consequently, the responded color palette arrays that were produced by varying concentrations and substances were unique. Thus, the results can be analyzed and evaluated to identify individual gases and their concentrations. For the quantitative analysis of color change, the color palette based on the ΔRGB intensity was analyzed for each chemical substance and concentration. In Figure 3a, the color palette arrays exhibit different color patterns corresponding to the interaction intensity of genetically engineered bacteriophages with the gas substance at the ppm scale concentration of four bacteriophage types at G_{20}. In addition, the color difference at G_{30} and G_{40} under VOCs exhibits a lower color distance than that observed in the G_{20} case in the color distance (detailed in Supporting Information Figure S5). Consequently, the plasmonic resonance strength strongly affects the color difference under the external stimulus of GPCF. To demonstrate the effect of AgNCs in the GPCF, we used two films with two different structures: with and without the AgNCs (as illustrated in Figure S6). The results imply that the GPCF can work well if AgNCs are present in the structure.

The fingerprint of the color patterns obtained by the color difference ΔE is presented in Figure 3b to investigate the selective response possibility. The results confirm that the cross-reaction of genetically engineered phages with a chemical substance can effectively distinguish between the VOC gases at

different concentrations through the particular shapes of each substance.

To analyze the VOC discrimination, a hierarchical cluster analysis was used as a multivariate analysis method to determine similarities across the ΔRGB intensity of a multiarray biosensor of these five chemical substances. The similarity of each chemical substance was performed using the Euclidean distance calculated by Ward's Linkage method. As illustrated in Figure 3c, the dendrograms of five chemical substances indicated that five VOC gases were accurately classified into five groups, even at a small concentration of 0.2 ppm in the hierarchical tree. This result of hierarchical cluster analysis (HCA) demonstrated that our GPCF film could selectively discriminate the VOC gases.

To understand the crucial function of coupling genetically engineered bacteriophages with variation in the bacteriophage thickness in multiarray biosensors, the classification success rates of bacteriophage-based sensors were calculated using HCA dendrograms (detailed in Supporting Information Figures S7 and S8. The multiarray biosensor is divided into seven groups marked as illustrated in Figure 4a, each with its own distinct characteristics. In groups 1, 2, and 3, the common property is the thickness of the bacteriophage coating; however, they are different in the type of genetically engineered bacteriophage. Conversely, the characteristics of bacteriophage thickness are different within the same group (in groups 4, 5, 6, and 7). From the heatmap of the classification success rate calculated from the HCA dendrogram of analyzed VOC data, all groups were not 100% distinguishable from all VOC gases, and within each group, one or more gases cannot be classified well. It is found that the classification success rate gradually decreases as the virus gap distance increases because of the resonance weakening between the AgNCs and metal mirror film (Figure 4b). Therefore, the color change of higher bacteriophage thickness is considerably weakened. In addition, the genetically engineered M13 phages exhibit high selectivity in interactions with VOCs, as represented by the heatmap. Each group represents a different virus (in groups 4, 5, 6, and 7), and it is impossible to distinguish all VOCs perfectly. However, the combination of genetically engineered bacteriophages and variation in the bacteriophage thickness strongly classifies substances that demonstrate the high efficiency of the
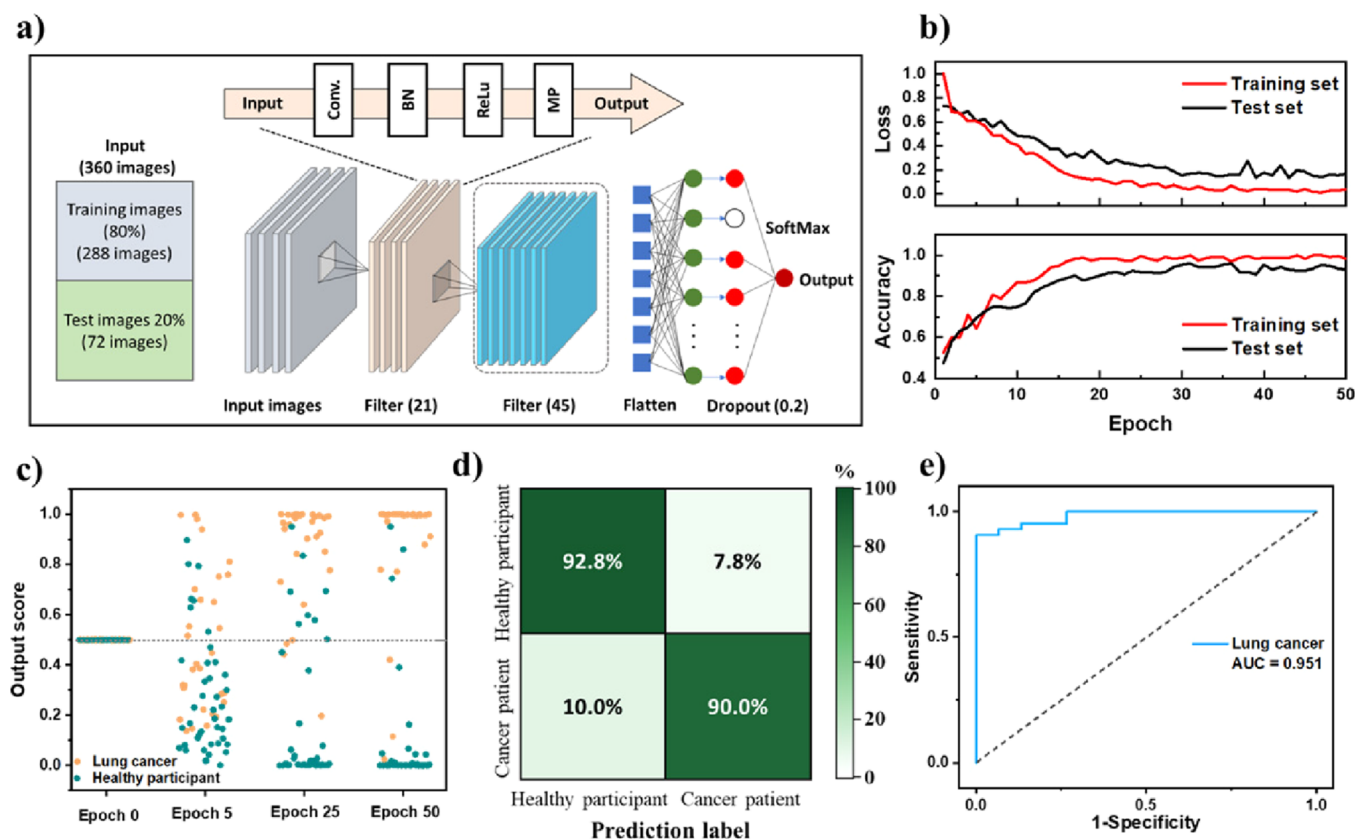
Figure 5. Deep-learning classification of lung cancer. (a) CNN model architecture used in this work. (b) Training, test loss, and accuracy. (c) Output of probabilities of prediction values for lung cancer patients and healthy participants. (d) Test accuracy values from lung cancer patients and healthy participants with CNN model prediction. (e) ROC curve and their AUC values.

multiarray biosensor in helping to distinguish VOC gases. Therefore, the multiarray biosensor based on the GPCF can be used in lung cancer diagnosis.

Lung Cancer Breath Sensing. Breath samples from the storage cabinet (4 °C) were taken outside and placed at room temperature for 20 min to ensure the same stability as sampling. The breath sample (10 mL) was sucked by a syringe from the collected breath (200 mL) and injected into a sealed chamber that was already pre-set with a multiarray biosensor. During analysis, the color difference was recorded using a CCD camera and was calculated in real time with the RGB values. The collected color differences from the multiarray sensor of each person were exhibited through fingerprinting patterns (Figure S9). Because human breathing is complex, noisy and contains only a very small number of endemic gases associated with lung disease, it is difficult to distinguish between healthy participants and patients using normal statistical and categorical methods. A machine learning model could be used for analyzing complex and noisy data. It is used as a computer tool to help analyze input data and produce accurately evaluated results (details in the Experimental Section). The convolutional neural network (CNN) model was used to classify the RGB data obtained during the breathing analysis of all the participants. The architecture of the CNN model was designed with two building blocks, including 21 filter layers and 45 filter layers (Figure 5a). Each building block comprises a series of convolutional layers (Conv) followed by BN, active function rectified linear unit (ReLu), and MP. Symbolic images were created from the RGB data representing diagnostic RGB data of each participant in the CNN input. The CNN model uses multiple filter layers to remove the background and clarify high abstractions that characterize each participant, thereby increasing the accuracy of the classification. In Figure 5b, the curves of loss and accuracy represent the learning process of the model with the training part and the test part. Consequently, there was no considerable difference between the training set and test set, showing the optimized model in training and evaluating data without overfitting issues.

After training 80% of the supplied data, the model was evaluated against the test data with the output of probability of prediction values from 0 to 1. The model indicated that the data were well classified upon training iterations (Figure 5c). By comparing the true label and prediction label with confidence prediction at the 0.5 thresholds, the CNN model achieved 90 and 92.8% accuracy for lung cancer patients and healthy participants, respectively (Figure 5d). The performance of the CNN model exhibited an average accuracy of 89.58% ± 3.16% with a fivefold cross-validation result (detailed in Table S3). Furthermore, our model achieved high performance in classifying lung cancer with an area under the curve (AUC) value of 0.951 by plotting a receiver operating characteristic (ROC) curve, as illustrated in Figure 5e. This design marks an essential milestone in developing a high-accuracy cancer diagnosis system using exhaled gas analysis, with the advantage of no pretreatment.

■ CONCLUSIONS

We have demonstrated a controllable GPCF for diagnosing lung cancer using human breath by exploiting the genetically

engineered M13 bacteriophage. The color-switching mechanism was obtained using an actuator of the M13 bacteriophage layer as a dielectric material in the gap plasmonic coupling film to tune reversibly via selective interactions of surface protein pVIII to the substances. A multiarray biosensor based on the GPCF was fabricated to detect humidity, and many functional VOC gases were observed distinctly via HCA to demonstrate the highly sensitive and selective ability. Moreover, we showed the importance of multiarray biosensors compared with separate groups through the classification success rate calculation. Our design has been studied to analyze and classify the breath samples of lung cancer patients and healthy participants. The output data from the multiarray biosensors were fed into the machine learning model as input data for training and evaluation. With the support of the machine learning and CNN model, the classification success rate of this design was more than 89% in classifying the breath of patients and healthy. We believe that our design can be easily fabricated with high selectivity, which will be applicable in designing novel devices for environmental protection and disease diagnosis.

■ EXPERIMENTAL SECTION

Fabrication of a Plasmonic Color Film Using Genetically Engineered M13 Bacteriophages. The genetically engineered bacteriophages were modified from the pVIII protein (major capsid) of wild-type into the (WHW) Trp-(W) His-(H) Trp-(W), (4E) Glu-(E) Glu-(E) Glu-(E), and (3A) Ala-(A) Ala-(A) Ala-(A), using site-directed mutagenesis (PCR) techniques.

To fabricate a plasmonic color film, a 100 nm-thick film of Ag deposited via electron-beam deposition on a Si substrate was cut into 1 × 1 cm pieces. Subsequently, the M13 bacteriophage layer was coated onto the Ag film using the spin-coating method (1500 rpm, 2 min). The thickness of the M13 bacteriophage layer at 20, 30, and 40 nm gap sizes was controlled by modifying the M13 bacteriophage concentration and determined using AFM. The polyvinylpyrrolidone-coated Ag nanocubes and nanoparticles of 75 m in diameter were bought from NanoComposix (SanDiego, CA 92111, USA). The nanoparticles were coated uniformly onto the M13 bacteriophage layer substrate using the spin-coating method (1500 rpm, 2 min).

Optical Measurements. The scattering spectra of all fabricated samples were measured using a commercial Olympus bright-field/DF microscope (BX53M) with a 100 × 0.9 NA objective under unpolarized halogen-light illumination. In addition, the scattering spectra were characterized using a fiber-optic spectrometer (US/USB4000, Ocean Optics, Dunedin, FL 34698, USA). The digital camera (16 megapixels) was connected to the microscope to capture the images to obtain the DF images.

AFM Measurements. An NX10 AFM system (Park Systems, Suwon, Korea) was used to examine the topography of the M13 surfaces and its swelling ability when humidity is absorbed in noncontact mode. The AFM was operated using the data acquisition program XEP 3.0.4 (Park Systems, Suwon, Korea). All data were analyzed using the XEI 1.8.2 image-processing program (Park Systems, Suwon, Korea). In addition, a specialized probe for noncontact mode was selected for measurements (PPP-NCHR, NANOSENSORS, Neuchatel, Switzerland).

Humidity and VOC Detection System. The gas sensing detection was tested using a home-built detection system.[33] The humidity levels were controlled from 20 to 90% in increments of 10%. All color was recorded and analyzed using a charged coupled device (CCD) video camera controlled by a MATLAB program which was used to manage the CCD video camera to capture the image and display the RGB values calculated in real time. To prevent external light interference, we conducted humidity detection in a dark room to accept simple LED lighting from the CCD camera. Initially, dry N_2 was passed through the chamber for humidity sensing preparation to

remove moisture. Then, the moisture flow from the humidifier was injected into the chamber controlled by a humidity sensor. The real-time color changes were analyzed as red, green, and blue (RGB) signals, and color images were captured every 3 s. The bacteriophage color changes were displayed and calculated based on RGB data difference between the initial color and phage color film at each relative humidity level using Photoshop (Adobe System Inc.). In similar processing, the VOC concentration of each substance was adjusted by controlling the volume solution of chemical substances. To obtain the stable condition of VOC concentration, the real-time color changes were analyzed in 3 min, and color images were captured every 3 s. The ΔRGB intensity and color difference (ΔE) in each capture were extracted based on the initial-state color.

Lung Cancer Breath Detection. *Breath Sample Collection Design.* Herein, exhaled breath samples were provided by Pusan National University, Yangsan Hospital Institutional Review Board, Yangsan, 50612, South Korea under protocol no.04-2018-035 and were practiced per the declaration of Helsinki. The total number of breath samples collected was 120, from lung cancer patients ($n = 50$) and healthy participants ($n = 70$) (detailed in Table S1). First, the patients were included in the analysis to diagnose lung cancer and the stage of cancer. The participating patients did not receive any cancer treatment before breath sampling. Second, lung cancer-negative healthy participants (through chest X-ray results) were recruited from Pusan National University campus participants. All participating patients and healthy participants gave informed consent before inclusion in this study.

All the participants were asked to rest well and fast for at least 8 h before taking their breath sample. Exhaled breath samples from patients and healthy participants were collected according to the European Respiratory Society technical standard recommendations. All the participants underwent bronchoscopy before taking the morning breath sample from 9:00 to 11:00 h. Breath samples from all the participants were collected through a 5-min gentle inhalation through the nose and exhalation through the mouth using a disposable mouthpiece into a 200-mL Tedlar sample bag. This mouthpiece has an internal filter design that helps prevent contamination from bacteria and virus. All the collected samples were stored in a fridge at 4 °C before being removed and analyzed.

Analysis. The analysis of breath samples from lung cancer patients and healthy participants was performed similarly to the analysis of VOCs. Exhaled breath samples were removed from the fridge and left in room temperature at least 20 min before being sucked by a syringe and injected directly into a chamber equipped with a multiarray biosensor. The color difference was recorded and calculated in real time with ΔRGB values.

CNN Model. The data-set used herein contains 360 samples (3 locations × 120 subjects) with a dimension of (360 × 7200) and includes 7200 unique features per sample (3 RGB values × 12 color films from multiarray biosensor ×200-time points). The data were randomly split into two parts: the training and test parts, with a splitting ratio of 80 and 20%, respectively. All data were pre-processed to fit the CNN model to the image input condition. The labels of healthy participants and patients were labeled as 0 and 1 to form a status column in the data, respectively. All input data are divided into four subgroups: x-train, y-train, x-test, and y-test, for items x-train and x-test as data containing 7200 unique features, and y-train and y-test as data of the state label column with two values 0 and 1. Because the input of the CNN model is an image, each sample is converted into a 2D shape using StandardScaler and fit transform functions configured from 7200 color arrays, which were transformed from 7200 unique features, as illustrated in Supplementary Figure S10. The simple CNN model architecture is illustrated in Figure 5a. Input images were fed into CNN structures, each with two building blocks that comprise a series of convolutional layers (Conv) followed by batch normalization (BN), active function ReLu, and max pooling (MP) layer. The output from the second convolutional layer was concatenated and passed to a single fully connected layer by Flatten, Dense function. Finally, the SoftMax function performs the network associated with a probability regression. The hyperparameters such as batch size, drop out, and the

number of filters in each convolutional layer used in the CNN model were optimized using the Bayesian optimization technique, as shown in Table S2. The training part and the test part were used independently in the CNN model. Accordingly, the training part (80% data) is used to train the model, and the test part (20% data) is used to evaluate the output of the model. The performance of the CNN model exhibited an average accuracy of 89.58% ± 3.16% with a fivefold cross-validation result (detailed in Table S3).

■ ASSOCIATED CONTENT

Supporting Information

The Supporting Information is available free of charge at https://pubs.acs.org/doi/10.1021/acssensors.2c02001.

Characterization of the GPCF, AFM analysis of the GPCF with relative humidity, color palette arrays with different humidity conditions, dark-field optical images under humidity conditions, color different patterns of VOC detection, Ag nanocube effect on the gap plasmonic color film, HCA of VOC analysis, fingerprinting patterns obtained from healthy participants and cancer patients, schematic diagram of pre-data processing for CNN, DNA sequencing of genetically engineered M13 phage, patient's baseline characteristics with lung cancer and healthy participant, and optimized hypermeter in the CNN model, and test accuracy values from the CNN model (PDF)

■ AUTHOR INFORMATION

Corresponding Authors

Kwang Ho Kim − School of Materials Science and Engineering and Global Frontier Research and Development Center for Hybrid Interface Materials, Pusan National University, Busan 46241, Republic of Korea; Email: kwhokim@pusan.ac.kr

Yun Seong Kim − Department of Internal Medicine, College of Medicine, Pusan National University, Pusan National University Yangsan Hospital, Yangsan 50612, Republic of Korea; Research Institute of Convergence Biomedical Science and Technology, Pusan National University Yangsan Hospital, Yangsan 50612, Republic of Korea; Email: yskim@pusan.ac.kr

Jin-Woo Oh − Bio-IT Fusion Technology Research Institute, Department of Nano Fusion Technology, Department of Nanoenergy Engineering and Research Center for Energy Convergence Technology, and Korea Nanobiotechnology Center, Pusan National University, Busan 46241, Republic of Korea; orcid.org/0000-0002-0065-5088; Email: ojw@pusan.ac.kr

Authors

Thanh Mien Nguyen − Bio-IT Fusion Technology Research Institute, Pusan National University, Busan 46241, Republic of Korea; orcid.org/0000-0002-8137-4455

Jae Heun Chung − Department of Internal Medicine, College of Medicine, Pusan National University, Pusan National University Yangsan Hospital, Yangsan 50612, Republic of Korea

Gyeong-Ha Bak − Department of Nano Fusion Technology, Pusan National University, Busan 46241, Republic of Korea

You Hwan Kim − Department of Nano Fusion Technology, Pusan National University, Busan 46241, Republic of Korea

Minjun Kim − Department of Physics, Chungnam National University, Daejeon 34134, Republic of Korea

Ye-Ji Kim − Department of Nano Fusion Technology, Pusan National University, Busan 46241, Republic of Korea; orcid.org/0000-0002-8710-6355

Ryuk Jun Kwon − Family Medicine Clinic and Research Institute of Convergence of Biomedical Science and Technology, Pusan National University Yangsan Hospital, Yangsan, Gyeongsangnam-do 50612, Republic of Korea

Eun-Jung Choi − Bio-IT Fusion Technology Research Institute and Korea Nanobiotechnology Center, Pusan National University, Busan 46241, Republic of Korea

Complete contact information is available at:
https://pubs.acs.org/10.1021/acssensors.2c02001

Author Contributions

¶T.M.N., J.H.C., and G.-H.B. contributed equally to this work.

Notes

The authors declare no competing financial interest.

■ ACKNOWLEDGMENTS

■ REFERENCES

(1) Jiang, N.; Zhuo, X.; Wang, J. Active Plasmonics: Principles, Structures, and Applications. Chem. Rev. 2018, 118, 3054−3099.

(2) Kim, J.-M.; Lee, C.; Lee, Y.; Lee, J.; Park, S.-J.; Park, S.; Nam, J.-M. Synthesis, Assembly, Optical Properties, and Sensing Applications of Plasmonic Gap Nanostructures. Adv. Mater. 2021, 33, No. 2006966.

(3) Liu, J.; Jalali, M.; Mahshid, S.; Wachsmann-Hogiu, S. Are plasmonic optical biosensors ready for use in point-of-need applications? Analyst 2020, 145, 364−384.

(4) Mejía-Salazar, J. R.; Oliveira, O. N., Jr. Plasmonic Biosensing. Chem. Rev. 2018, 118, 10617−10625.

(5) Montelongo, Y.; Tenorio-Pearl, J. O.; Williams, C.; Zhang, S.; Milne, W. I.; Wilkinson, T. D. Plasmonic nanoparticle scattering for color holograms. Proc. Natl. Acad. Sci. U. S. A. 2014, 111, 12679−12683.

(6) Tittl, A.; Giessen, H.; Liu, N. Plasmonic gas and chemical sensing. NANO 2014, 3, 157−180.

(7) Moreau, A.; Ciracì, C.; Mock, J. J.; Hill, R. T.; Wang, Q.; Wiley, B. J.; Chilkoti, A.; Smith, D. R. Controlled-reflectance surfaces with film-coupled colloidal nanoantennas. Nature 2012, 492, 86−89.

(8) Mock, J. J.; Hill, R. T.; Degiron, A.; Zauscher, S.; Chilkoti, A.; Smith, D. R. Distance-Dependent Plasmon Resonant Coupling between a Gold Nanoparticle and Gold Film. Nano Lett. 2008, 8, 2245−2252.

(9) Hill, R. T.; Mock, J. J.; Urzhumov, Y.; Sebba, D. S.; Oldenburg, S. J.; Chen, S.-Y.; Lazarides, A. A.; Chilkoti, A.; Smith, D. R. Leveraging Nanoscale Plasmonic Modes to Achieve Reproducible Enhancement of Light. Nano Lett. 2010, 10, 4150−4154.

(10) Hill, R. T.; Mock, J. J.; Hucknall, A.; Wolter, S. D.; Jokerst, N. M.; Smith, D. R.; Chilkoti, A. Plasmon Ruler with Angstrom Length Resolution. ACS Nano 2012, 6, 9237−9246.

(11) Lassiter, J. B.; McGuire, F.; Mock, J. J.; Ciracì, C.; Hill, R. T.; Wiley, B. J.; Chilkoti, A.; Smith, D. R. Plasmonic Waveguide Modes of Film-Coupled Metallic Nanocubes. Nano Lett. 2013, 13, 5866−5872.

(12) Devaraj, V.; Jeong, N.-N.; Lee, J.-M.; Hwang, Y.-H.; Sohn, J.-R.; Oh, J.-W. Revealing Plasmonic Property Similarities and Differences Between a Nanoparticle on a Metallic Mirror and Free Space Dimer Nanoparticle. J. Korean Phys. Soc. 2019, 75, 313−318.

(13) Ding, F.; Yang, Y.; Deshpande, R. A.; Bozhevolnyi, S. I. A review of gap-surface plasmon metasurfaces: fundamentals and applications. *NANO* **2018**, *7*, 1129−1156.

(14) Huynh, L. T. M.; Yoon, S. Patterning Nanogaps: Spatial Control of the Distribution of Nanogaps between Gold Nanoparticles and Gold Substrates. *J. Phys. Chem. C* **2018**, *122*, 26047−26053.

(15) Srivastava, S. K.; Li, A.; Li, S.; Abdulhalim, I. Optimal Interparticle Gap for Ultrahigh Field Enhancement by LSP Excitation via ESPs and Confirmation Using SERS. *J. Phys. Chem. C* **2016**, *120*, 28735−28742.

(16) Abutoama, M.; Isaacs, S.; Ney, M.; Zhong, L.; Li, D.; Jiang, L.; Abdulhalim, I. Ultrahigh Field Enhancement Optimization Versus Rabi Splitting Investigated Using Au Nano-Bipyramids on Metal Films. *J. Phys. Chem. C* **2019**, *123*, 12984−12996.

(17) Abdulhalim, I. Coupling configurations between extended surface electromagnetic waves and localized surface plasmons for ultrahigh field enhancement. *Nanophotonics* **2018**, *7*, 1891−1916.

(18) Abhilash, T.; Balasubrahmaniyam, M.; Patra, A.; Kasiviswanathan, S. Plasmon resonance mediated enhancement in Fabry-Pérot cavity modes. *Appl. Phys. Lett.* **2014**, *104*, 241112.

(19) Seok, T. J.; Jamshidi, A.; Kim, M.; Dhuey, S.; Lakhani, A.; Choo, H.; Schuck, P. J.; Cabrini, S.; Schwartzberg, A. M.; Bokor, J.; Yablonovitch, E.; Wu, M. C. Radiation Engineering of Optical Antennas for Maximum Field Enhancement. *Nano Lett.* **2011**, *11*, 2606−2610.

(20) Kim, M.; Kwon, H.; Lee, S.; Yoon, S. Effect of Nanogap Morphology on Plasmon Coupling. *ACS Nano* **2019**, *13*, 12100−12108.

(21) Barnes, W. L.; Dereux, A.; Ebbesen, T. W. Surface plasmon subwavelength optics. *Nature* **2003**, *424*, 824−830.

(22) Shen, J.; Luan, B.; Pei, H.; Yang, Z.; Zuo, X.; Liu, G.; Shi, J.; Wang, L.; Zhou, R.; Cheng, W.; Fan, C. Humidity-Responsive Single-Nanoparticle-Layer Plasmonic Films. *Adv. Mater.* **2017**, *29*, No. 1606796.

(23) Powell, A. W.; Coles, D. M.; Taylor, R. A.; Watt, A. A. R.; Assender, H. E.; Smith, J. M. Plasmonic Gas Sensing Using Nanocube Patch Antennas. *Adv. Opt. Mater.* **2016**, *4*, 634−642.

(24) Qin, J.; Chen, Y.-H.; Ding, B.; Blaikie, R. J.; Qiu, M. Efficient Plasmonic Gas Sensing Based on Cavity-Coupled Metallic Nano-particles. *J. Phys. Chem. C* **2017**, *121*, 24740−24744.

(25) Shrivastav, A. M.; Cvelbar, U.; Abdulhalim, I. A comprehensive review on plasmonic-based biosensors used in viral diagnostics. *Commun. Biol.* **2021**, *4*, 70.

(26) Anker, J. N.; Hall, W. P.; Lyandres, O.; Shah, N. C.; Zhao, J.; Van Duyne, R. P. Biosensing with plasmonic nanosensors. *Nat. Mater.* **2008**, *7*, 442−453.

(27) Lee, J. H.; Hwang, J. H.; Nam, J. M. DNA-tailored plasmonic nanoparticles for biosensing applications. *Wiley Interdiscip. Rev. Nanomed. Nanobiotechnol.* **2013**, *5*, 96−109.

(28) James, T. D.; Mulvaney, P.; Roberts, A. The Plasmonic Pixel: Large Area, Wide Gamut Color Reproduction Using Aluminum Nanostructures. *Nano Lett.* **2016**, *16*, 3817−3823.

(29) Ding, T.; Sigle, D.; Zhang, L.; Mertens, J.; de Nijs, B.; Baumberg, J. Controllable Tuning Plasmonic Coupling with Nano-scale Oxidation. *ACS Nano* **2015**, *9*, 6110−6118.

(30) Ding, T.; Rüttiger, C.; Zheng, X.; Benz, F.; Ohadi, H.; Vandenbosch, G. A. E.; Moshchalkov, V. V.; Gallei, M.; Baumberg, J. J. Fast Dynamic Color Switching in Temperature-Responsive Plasmonic Films. *Adv. Opt. Mater.* **2016**, *4*, 877−882.

(31) Liu, L.; Aleisa, R.; Zhang, Y.; Feng, J.; Zheng, Y.; Yin, Y.; Wang, W. Dynamic Color-Switching of Plasmonic Nanoparticle Films. *Angew. Chem., Int. Ed.* **2019**, *58*, 16307−16313.

(32) Lee, S.; Sim, K.; Moon, S. Y.; Choi, J.; Jeon, Y.; Nam, J.-M.; Park, S.-J. Controlled Assembly of Plasmonic Nanoparticles: From Static to Dynamic Nanostructures. *Adv. Mater.* **2021**, *33*, No. 2007668.

(33) Oh, J.-W.; Chung, W.-J.; Heo, K.; Jin, H.-E.; Lee, B. Y.; Wang, E.; Zueger, C.; Wong, W.; Meyer, J.; Kim, C.; Lee, S. Y.; Kim, W. G.; Zemla, M.; Auer, M.; Hexemer, A.; Lee, S. W. Biomimetic virus-based colourimetric sensors. *Nat. Commun.* **2014**, *5*, 3043.

(34) Moon, J.-S.; Lee, Y.; Shin, D.-M.; Kim, C.; Kim, W.-G.; Park, M.; Han, J.; Song, H.; Kim, K.; Oh, J.-W. Identification of Endocrine Disrupting Chemicals using a Virus-Based Colorimetric Sensor. *Chem. − Asian J.* **2016**, *11*, 3097−3101.

(35) Lee, J. H.; Fan, B.; Samdin, T. D.; Monteiro, D. A.; Desai, M. S.; Scheideler, O.; Jin, H.-E.; Kim, S.; Lee, S.-W. Phage-Based Structural Color Sensors and Their Pattern Recognition Sensing System. *ACS Nano* **2017**, *11*, 3632−3641.

(36) Yoo, Y. J.; Kim, W.-G.; Ko, J. H.; Kim, Y. J.; Lee, Y.; Stanciu, S. G.; Lee, J.-M.; Kim, S.; Oh, J.-W.; Song, Y. M. Large-Area Virus Coated Ultrathin Colorimetric Sensors with a Highly Lossy Resonant Promoter for Enhanced Chromaticity. *Adv. Sci.* **2020**, *7*, No. 2000978.

(37) Lee, J.-M.; Devaraj, V.; Jeong, N.-N.; Lee, Y.; Kim, Y.-J.; Kim, T.; Yi, S. H.; Kim, W.-G.; Choi, E. J.; Kim, H.-M.; Chang, C. L.; Mao, C.; Oh, J.-W. Neural mechanism mimetic selective electronic nose based on programmed M13 bacteriophage. *Biosens. Bioelectron.* **2022**, *196*, No. 113738.

(38) Nguyen, T. M.; Kim, W.-G.; Ahn, H.-J.; Kim, M.; Kim, Y. D.; Devaraj, V.; Kim, Y.-J.; Lee, Y.; Lee, J.-M.; Choi, E. J.; Oh, J.-W. Programmable self-assembly of M13 bacteriophage for micro-color pattern with a tunable colorization. *RSC Adv.* **2021**, *11*, 32305−32311.

(39) Cao, B.; Li, Y.; Yang, T.; Bao, Q.; Yang, M.; Mao, C. Bacteriophage-based biomaterials for tissue regeneration. *Adv. Drug Deliv. Rev.* **2019**, *145*, 73−95.

(40) Yan, Y.; Kim, W.-G.; Ma, X.; Tegafaw, T.; Nguyen, T. M.; Lee, J.-M.; Choi, E.-J.; Ahn, H.; Ha, S.-H.; Kim, K.; Kim, J.-M.; Kim, H. K.; Oh, J.-W.; Shin, D.-M.; Hwang, Y.-H. Nanogenerators facilitated piezoelectric and flexoelectric characterizations for bioinspired energy harvesting materials. *Nano Energy* **2021**, *81*, No. 105607.

(41) Lee, J. H.; Warner, C. M.; Jin, H.-E.; Barnes, E.; Poda, A. R.; Perkins, E. J.; Lee, S.-W. Production of tunable nanomaterials using hierarchically assembled bacteriophages. *Nat. Protoc.* **2017**, *12*, 1999−2013.

(42) Chung, W.-J.; Oh, J.-W.; Kwak, K.; Lee, B. Y.; Meyer, J.; Wang, E.; Hexemer, A.; Lee, S.-W. Biomimetic self-templating supra-molecular structures. *Nature* **2011**, *478*, 364−368.

(43) Yang, S. H.; Chung, W.-J.; McFarland, S.; Lee, S.-W. Assembly of Bacteriophage into Functional Materials. *Chem. Rec.* **2013**, *13*, 43−59.

(44) Lee, J. M.; Choi, E. J.; Chung, J. H.; Lee, K. W.; Lee, Y.; Kim, Y. J.; Kim, W. G.; Yoon, S. H.; Seol, H. Y.; Devaraj, V.; Ha, J. S.; Lee, D.; Kwon, S. M.; Kim, Y. S.; Chang, C. L.; Oh, J. W. A DNA-derived phage nose using machine learning and artificial neural processing for diagnosing lung cancer. *Biosens. Bioelectron.* **2021**, *194*, No. 113567.

(45) Nguyen, T. M.; Kim, S.-J.; Devaraj, V.; Song, H.; Lee, J.-M.; Choi, E. J.; Kim, Y.-J.; Jang, M.; Kim, Y. H.; Jeong, H.; Kim, C.-S.; Kim, K.; Oh, J.-W. Biomaterial actuator of M13 bacteriophage in dynamically tunable plasmonic coupling structure. *Sens. Actuators B Chem.* **2022**, *369*, No. 132326.

(46) Saalberg, Y.; Wolff, M. VOC breath biomarkers in lung cancer. *Clin. Chim. Acta* **2016**, *459*, 5−9.